JOURNAL OF COMPUTATIONAL PHYSICS 99, 233–250 (1992)

Upwind Differencing and LU Factorization for Chemical Non-equilibrium Navier–Stokes Equations

JIAN-SHUN SHUEN

Sverdrup Technology, Inc., NASA Lewis Research Center, Cleveland, Ohio 44135

Received January 10, 1990; revised March 28, 1991

An efficient and robust upwind method for solving the chemical non-equilibrium Navier–Stokes equations has been developed. The method uses either the Roe or Van Leer flux-splitting for inviscid terms and central differencing for viscous terms in the explicit operator (residual), and the Steger–Warming (SW) splitting and lower–upper (LU) approximate factorization for the implicit operator. This approach is efficient since the SW–LU combination requires the inversion of only block diagonal matrices, as opposed to the block tridiagonal inversion of the widely used ADI method, and is fully vectorizable. The LU method is particularly advantageous for systems with large number of equations, such as for chemical and thermal nonequilibrium flow. Formulas of the numerical method are presented for the finite-volume discretization of the Navier–Stokes equations in general coordinates. Numerical tests in hypersonic blunt body, ramped-duct, shock wave/boundary layer interaction, and divergent nozzle flows demonstrate the efficiency and robustness of the present method.

1. INTRODUCTION

Maximizing accuracy, efficiency, and robustness has been the primary goal for designing algorithms in numerical analysis. This is especially important for solution of the complex multi-dimensional Navier–Stokes equations which may include a large system of chemical reactions and other models such as turbulence equations. In the past there have been two approaches to solving the reacting flow governing equation set. One approach is to decouple the flow equations from the species (and nonequilibrium thermal energy) equations and solve them separately by either an implicit or explicit method [1]. This approach has the advantage that it is relatively easy to implement and that the flow and species equation sets may be solved using different schemes. However, for flows with very significant nonequilibrium effects and large thermal energy changes due to heat release or absorption, the decoupled approach is likely to be less robust and may encounter difficulties in convergence. The second approach involves solving all the equations in a simultaneous, coupled manner [2–4]. In Refs. [2–4] coupled, implicit algorithms are successfully used to solve thermo-chemical nonequilibrium flow problems.

Recently upwind schemes [5–7] have achieved recognition for their capability of yielding accurate representation of discontinuities and for the sound theoretical basis of characteristic theory of hyperbolic systems. Liou and Van Leer [8] compared several prominent flux splitting schemes for a wide range of problems regarding their accuracy and efficiency. With the renewed interest in high-temperature and chemically reacting flows, these methods have recently been extended to real gases by several researchers [9–15].

Since the mid-seventies, the ADI method developed by Beam and Warming [16] has become popular and led to the successful development of the well-known ARC3D code that has demonstrated itself as a viable method for treating many aerodynamic problems involving ideal gases. However, a major deficiency of the ADI method is the unconditional instability in delta form in three dimensions, resulting from the factorization error. The instability is from a linear analysis and without boundary conditions taken into account. In practice the approach does work, provided that appropriate amount of artificial damping is added. The ADI method requires the inversion of large block banded (tridiagonal or pentadiagonal) matrices, which can be very costly when a large number of species/thermal energy equations are solved along with flow equations in chemical/thermal nonequilibrium flows. Instead of splitting the implicit operator into three factors (in three-dimensional problems), Jameson and Turkel [17] constructed an LU scheme that requires only two factors involving lower (L) and upper (U) triangular matrices. Based on the same principle, Steger and Warming [5] independently developed an LU factorization procedure for their flux-splitting method for ideal gases. The LU scheme is unconditionally stable in any number of spatial dimensions and yields a steady-state solution independent of time step. Unlike the block banded diagonal system resulting from the ADI scheme, the LU scheme results in a block diagonal system for which the computational effort is moderate. Furthermore, the scheme can easily take full

0021-9991/92 $3.00

advantage of vectorization in the solution of the LU factors, avoiding the recursive procedure occurring in the banded diagonal system. Consequently, the LU scheme is an attractive method for reacting flows where the block size is large due to the presence of species equations and deserves further attention.

In some of the earlier work on LU factorization [3, 18, 19], the explicit (residual) operator is constructed using central difference, the implicit operator, on the other hand, using one-sided difference. Although a one-sided difference is used for the implicit operator, it does not constitute an upwind scheme. This is because the splitting of the inviscid flux Jacobian matrices in these studies is not obtained according to the directions of wave propagation. Reference [5] is a notable exception in that both the implicit and explicit operators are constructed using an upwind method, but only for perfect-gas flows. Therefore, it is natural to ask the questions—how does one apply the LU approximation to modern upwind schemes, especially for reacting flows, and how well do these resulting schemes perform in practice?

It is our objective in this paper to develop a new procedure that combines the accuracy of modern upwind schemes and the efficiency of the LU scheme for chemical nonequilibrium flows. In the next section, we briefly discuss the governing equations and real-gas properties for chemical nonequilibrium flows. The derivation of split-flux formulas and viscous formulation are given in Section 3. Then in Section 4 we describe the development of the LU implicit algorithm. Finally, in Section 5 we show numerical results for hypersonic blunt body, ramped-duct, shock wave/boundary layer interaction, and divergent nozzle flows. Only laminar flows are considered in the present study.

2. GOVERNING EQUATIONS

The two-dimensional, Navier–Stokes and species transport equations for a chemically reacting gas of N species are given by

$$\frac{\partial \mathbf{U}}{\partial t}+\frac{\partial \mathbf{F}}{\partial x}+\frac{\partial \mathbf{G}}{\partial y}-\frac{\partial \mathbf{F}_v}{\partial x}-\frac{\partial \mathbf{G}_v}{\partial y}=\mathbf{S}, \tag{1}$$

where

$$\mathbf{U}=\begin{bmatrix}\rho\\ \rho u\\ \rho v\\ \rho E\\ C_1\\ C_2\\ \vdots\\ C_{N-1}\end{bmatrix},\qquad \mathbf{F}=\begin{bmatrix}\rho u\\ \rho u^2+p\\ \rho uv\\ u(\rho E+p)\\ uC_1\\ uC_2\\ \vdots\\ uC_{N-1}\end{bmatrix},$$

$$\mathbf{G}=\begin{bmatrix}\rho v\\ \rho uv\\ \rho v^2+p\\ v(\rho E+p)\\ vC_1\\ vC_2\\ \vdots\\ vC_{N-1}\end{bmatrix},\qquad \mathbf{F}_v=\begin{bmatrix}0\\ \tau_{xx}\\ \tau_{xy}\\ \Omega_x\\ -C_1\tilde{u}_1\\ -C_2\tilde{u}_2\\ \vdots\\ -C_{N-1}\tilde{u}_{N-1}\end{bmatrix},$$

$$\mathbf{G}_v=\begin{bmatrix}0\\ \tau_{xy}\\ \tau_{yy}\\ \Omega_y\\ -C_1\tilde{v}_1\\ -C_2\tilde{v}_2\\ \vdots\\ -C_{N-1}\tilde{v}_{N-1}\end{bmatrix},\qquad \mathbf{S}=\begin{bmatrix}0\\ 0\\ 0\\ 0\\ S_1\\ S_2\\ \vdots\\ S_{N-1}\end{bmatrix}.$$

$$\tau_{xx}=2\mu\frac{\partial u}{\partial x}-\frac{2}{3}\mu\left(\frac{\partial u}{\partial x}+\frac{\partial v}{\partial y}\right),$$

$$\tau_{xy}=\mu\left(\frac{\partial u}{\partial y}+\frac{\partial v}{\partial x}\right),$$

$$\tau_{yy}=2\mu\frac{\partial v}{\partial y}-\frac{2}{3}\mu\left(\frac{\partial u}{\partial x}+\frac{\partial v}{\partial y}\right),$$

$$\Omega_x=u\tau_{xx}+v\tau_{xy}+k\frac{\partial T}{\partial x}-\sum_{i=1}^{N}h_iC_i\tilde{u}_i,$$

$$\Omega_y=u\tau_{xy}+v\tau_{yy}+k\frac{\partial T}{\partial y}-\sum_{i=1}^{N}h_iC_i\tilde{v}_i.$$

In these equations, the physical variables are the density ρ, the velocity components (u, v), the pressure p, the temperature T, the internal energy e, and the total energy $E=e+\frac{1}{2}(u^2+v^2)$. The mass concentration and enthalpy of species i are respectively C_i and h_i, and μ and k are molecular viscosity and thermal conductivity, respectively, of the gas mixture. The source term for species i due to chemical reactions is S_i, and $\tilde{u}_i$ and $\tilde{v}_i$ are the diffusion velocities of species i in the x- and y-direction, respectively, which are found by Fick's law:

$$Y_i\tilde{u}_i=-D_{im}\frac{\partial Y_i}{\partial x},$$

$$Y_i\tilde{v}_i=-D_{im}\frac{\partial Y_i}{\partial y},$$

where $Y_i=C_i/\rho$ is the mass fraction of species i, $D_{im}=(1-X_i)/\sum_{j\neq i}^{N}X_j/D_{ij}$ is the effective binary diffusivity of species i in the gas mixture, obtained by treating the

species i and the surrounding gas as a binary mixture [20], and X_i is the molar fraction of species i. It should be noted that Fick's law is a convenient approximation of the multicomponent diffusion equations obtained from the kinetic theory of gases. The validity of this approximation is discussed in detail in [20].

In reacting flow calculations, the evaluation of thermophysical properties is of vital importance. In this paper, the specific heat C_p, thermal conductivity k, and viscosity μ for each species are determined by fourth-order polynomials of temperature. The coefficients of these polynomials were obtained from [21] and are valid up to a temperature of 10,000 K. The specific heat of the gas mixture is obtained by mass concentration weighting of individual species. The thermal conductivity and viscosity of the mixture, however, are calculated using Wilke's mixing rule [22]. The binary mass diffusivity D_{ij} between species i and j is obtained using the Chapman–Enskog theory [22].

To close the system of equations, Eq. (1), we need to define the equation of state. We begin by assuming that the macroscopic thermodynamic properties of the gas are related through the general equation of state,

$$p = p(\rho, e, C_1, C_2, ..., C_{N-1}). \tag{2}$$

We note that, since the total mass density is already included, only $N-1$ species are independent for a chemical system of N species. If we further assume that the intermolecular forces and the volume occupied by molecules are negligible, the gas mixture pressure p may be expressed as the sum of the partial pressure due to each species in the ideal-gas relation:

$$p = R_u T \sum_{i=1}^{N} \frac{C_i}{W_i}, \tag{3}$$

where R_u is the universal gas constant and W_i is the molecular weight of species i. The temperature T appearing in the above equations is obtained from the enthalpy relationship,

$$h = \sum_{i=1}^{N} Y_i h_i = \sum_{i=1}^{N} Y_i \left(h_{fi}^{\circ} + \int_{T_R}^{T} C_{p_i}\, dT \right), \tag{4}$$

and h_{fi}° and C_{p_i} are the heat of formation and constant pressure specific heat of species i, respectively; T_R is the reference temperature for thermodynamic properties.

The flux-splitting formulation in the present paper requires the definition of the (frozen) speed of sound and pressure derivatives p_ρ, p_e, and p_{C_i} (the partial derivatives of p with respect to ρ, e, and C_i, respectively, while holding other variables fixed). These quantities can be obtained from the equation of state as follows:

$$a^2 \equiv \left(\frac{\partial p}{\partial \rho}\right)_s = p_\rho + \frac{p_e p}{\rho^2} + \sum_{i=1}^{N-1} \frac{C_i}{\rho} p_{C_i} \tag{5}$$

$$p_\rho = \left(\frac{\partial p}{\partial \rho}\right)_{e, C_i, i=1, N-1} = \frac{R_u T}{W_n} + \frac{R_u}{W C_v} \sum_{i=1}^{N-1} \frac{C_i}{\rho} (e_i - e_N), \tag{6a}$$

$$p_e = \left(\frac{\partial p}{\partial e}\right)_{\rho, C_i, i=1, N-1} = \frac{\rho R_u}{W C_v}, \tag{6b}$$

$$p_{C_i} = \left(\frac{\partial p}{\partial C_i}\right)_{\rho, e, C_j, j=1, N-1, j \neq i} = R_u T \left(\frac{1}{W_i} - \frac{1}{W_N}\right) - \frac{R_u}{W C_v} (e_i - e_N), \tag{6c}$$

where $W = ((1/\rho) \sum_{i=1}^{N} (C_i/W_i))^{-1}$ is the molecular weight of the gas mixture, $C_v = \sum_{i=1}^{N} C_i C_{p_i}/\rho - R_u/W$ is the constant-volume specific heat of the gas mixture, and $e_i = \int_{T_R}^{T} C_{p_i}\, dT + h_{fi}^{\circ} - R_u T/W_i$ is the specific internal energy of the ith species.

The finite-rate chemistry model used in the present calculations includes five species (O_2, N_2, O, N, NO) and 11 elementary reaction steps for the dissociation and recombination of air. The reactions and the rate coefficients are taken from Dunn and Kang [23].

3. EXPLICIT (RESIDUAL) OPERATOR

3.1. *Roe Splitting*

To construct Roe flux-difference splitting, one usually defines an average state $\hat{\mathbf{U}}$ such that the flux differences between two neighboring states, denoted by "**L**" and "**R**", are related to the differences in state variables by (for the x-direction):

$$\Delta \mathbf{F} = \hat{\mathbf{A}}\, \Delta \mathbf{U}, \tag{7}$$

where

$$\Delta(\cdot) = (\cdot)_{\mathbf{R}} - (\cdot)_{\mathbf{L}}, \qquad \hat{\mathbf{A}} = \mathbf{A}(\hat{\mathbf{U}}), \qquad \mathbf{A}(\mathbf{U}) = \partial \mathbf{F}/\partial \mathbf{U}$$

and

$$\hat{\mathbf{U}} = \hat{\mathbf{U}}(\mathbf{U}_{\mathbf{L}}, \mathbf{U}_{\mathbf{R}}).$$

The object now is to find an average state known as the Roe-average state, such that Eq. (7) is satisfied exactly for all admissible pairs $(\mathbf{U}_{\mathbf{L}}, \mathbf{U}_{\mathbf{R}})$. In the case of a calorically perfect gas this is easily accomplished, since Eq. (7)

represents four relatively simple equations with four unknowns in $\hat{\mathbf{U}}$ (in two dimensions). For a reacting gas, the simplicity is lost and the definition of the average state is non-unique. In [14, 15], sets of average variables are derived for both chemical equilibrium and nonequilibrium flows, which are shown to be consistent and to work well.

Since the eigenvalues of the Jacobian matrix $\mathbf{A}$ are real [15], the splitting of these eigenvalues according to their signs leads to the splitting of $\mathbf{A}$:

$$\mathbf{A} = \mathbf{A}^+ + \mathbf{A}^-. \tag{8a}$$

Thus, the flux difference can be split accordingly,

$$\Delta\mathbf{F} = \Delta\mathbf{F}^+ + \Delta\mathbf{F}^-, \qquad \Delta\mathbf{F}^\pm = \hat{\mathbf{A}}^\pm \Delta\mathbf{U}. \tag{8b}$$

The split flux differences $\Delta\mathbf{G}^\pm$ and the flux Jacobian matrices $\mathbf{B}$, $\mathbf{B}^\pm$, and $\hat{\mathbf{B}}^\pm$ in the y-direction are defined similarly.

Although the Roe splitting in Cartesian coordinates can be easily constructed, it requires special care in general coordinates, where geometric metrics are involved in the formulation. We note that the Roe-average variables should be obtained independent of geometric quantities and the metrics at the cell interface are to be used in the evaluation of split fluxes.

In general coordinates (ξ, η, ζ), the interface flux is represented by the inner product of the Cartesian flux vector and the surface unit vector. Specifically, the inviscid flux in the ξ-direction, $\tilde{\mathbf{F}}$, in 2D general coordinates (ξ, η) can be written as

$$\tilde{\mathbf{F}} = \frac{(y_\eta \mathbf{F} - x_\eta \mathbf{G})}{\sqrt{x_\eta^2 + y_\eta^2}}, \tag{9a}$$

and the Jacobian

$$\tilde{\mathbf{A}} = \frac{\partial \tilde{\mathbf{F}}}{\partial \mathbf{U}} = \frac{(y_\eta \mathbf{A} - x_\eta \mathbf{B})}{\sqrt{x_\eta^2 + y_\eta^2}}, \tag{9b}$$

where x_η and y_η are covariant metrics evaluated at the interface, and $\sqrt{x_\eta^2 + y_\eta^2}$ is the cell interface area (length in 2D). The inviscid flux $\tilde{\mathbf{G}}$ and flux Jacobian $\tilde{\mathbf{B}}$ in the η-direction are obtained by replacing y_η and x_η with $-y_\xi$ and $-x_\xi$, respectively, in Eqs. (9a) and (9b).

Next, we turn to the derivation of split fluxes via splitting matrices. Warming, Beam, and Hyett [24] showed that a combination of component Jacobians for inviscid fluxes is diagonalizable, specifically

$$\hat{\mathbf{A}} = \mathbf{S}_\xi \Lambda_\xi \mathbf{S}_\xi^{-1}, \tag{10}$$

where Λ_ξ contains the (real) eigenvalues of $\tilde{\mathbf{A}}$, i.e.,

$$\begin{aligned} \Lambda_\xi &= \mathrm{diag}(\lambda_\xi), \\ \lambda_\xi(\tilde{\mathbf{A}}) &= u_\xi, u_\xi, u_\xi + a, u_\xi - a, u_\xi, \ldots, u_\xi, \\ u_\xi &= \frac{(y_\eta u - x_\eta v)}{\sqrt{x_\eta^2 + y_\eta^2}}. \end{aligned} \tag{11}$$

$\mathbf{S}_\xi$ and $\mathbf{S}_\xi^{-1}$ are similarity matrices and are composed of the right and left eigenvectors of $\tilde{\mathbf{A}}$, respectively. The matrix $\mathbf{S}_\xi$ and its inverse $\mathbf{S}_\xi^{-1}$ are frequently used in numerical flux functions and are given in the Appendix for a chemical nonequilibrium gas in general coordinates.

For clarity of presentation, in the derivation of similarity matrices and the rest of the paper we have set $N = 5$, which is the number of species considered in our chemistry model. Following the same procedure as in the case of Cartesian coordinates, one finds the splitting of the Jacobian matrix $\tilde{\mathbf{A}}$ in general coordinates,

$$\tilde{\mathbf{A}} = \tilde{\mathbf{A}}^+ + \tilde{\mathbf{A}}^-, \qquad \tilde{\mathbf{A}}^\pm = \mathbf{S}_\xi \Lambda_\xi^\pm S_\xi^{-1}, \tag{12}$$

where $\Lambda_\xi^\pm = \mathrm{diag}[(\lambda_{\xi_i} \pm |\lambda_{\xi_i}|)/2]$. This leads to the splitting of the flux difference,

$$\Delta\tilde{\mathbf{F}} = \Delta\tilde{\mathbf{F}}^+ + \Delta\tilde{\mathbf{F}}^- \tag{13a}$$

and

$$\Delta\tilde{\mathbf{F}}^\pm = \hat{\tilde{\mathbf{A}}}^\pm \Delta\mathbf{U}. \tag{13b}$$

The split fluxes in the η-direction, $\Delta\tilde{\mathbf{G}}^\pm$, can be similarly obtained. We note that in the above derivation only flow properties in the L and R cells are used in the evaluation of the Roe-average state (Eq. (7)), i.e., the metrics are not involved. Note, further, that cell interface metrics are used in the similarity matrices and the diagonalization procedure.

3.2. *Van Leer Splitting*

In our previous studies [14, 15], we have extended the Van Leer splitting to a general equilibrium gas and a gas not in chemical equilibrium for 1D flows. The further generalization of the splitting to 2D general coordinates is straightforward; the formulas are given below.

The splitting in the ξ-direction has the standard form

$$\tilde{\mathbf{F}} = \tilde{\mathbf{F}}^+ + \tilde{\mathbf{F}}^-, \tag{14}$$

and is carried out only when the eigenvalues have mixed signs, i.e., when $M_\xi^2 < 1$ for the system of Eq. (1) with

eigenvalues given by Eq. (11) ($M_\xi = u_\xi/a$ is the local Mach number). The split mass, momentum, and energy fluxes are

$$\tilde{\mathbf{F}}_1^{\pm} = \pm \tfrac{1}{4}\rho a(M_\xi \pm 1)^2, \tag{15a}$$

$$\tilde{\mathbf{F}}_2^{\pm} = \tilde{\mathbf{F}}_1^{\pm}\left[u - \frac{y_\eta}{\sqrt{x_\eta^2 + y_\eta^2}}\frac{p}{\rho a^2}(u_\xi \mp 2a)\right], \tag{15b}$$

$$\tilde{\mathbf{F}}_3^{\pm} = \tilde{\mathbf{F}}_1^{\pm}\left[v + \frac{x_\eta}{\sqrt{x_\eta^2 + y_\eta^2}}\frac{p}{\rho a^2}(u_\xi \mp 2a)\right], \tag{15c}$$

$$\mathbf{F}_4^{\pm} = \tilde{\mathbf{F}}_1^{\pm}[H - m(u_\xi \mp a)^2], \tag{15d}$$

where H is the specific total enthalpy. Exactly as in the 1D case [14, 15], the parameter m generates a family of splittings; Van Leer's splitting is a member of this family, found by requiring that the terms in the square bracket of the $\tilde{\mathbf{F}}_4^{\pm}$ fluxes form a perfect square. This leads to

$$m = h\Big/\left(a^2 + 2h\frac{u_\xi^2}{u^2 + v^2}\right).$$

To avoid an indeterminate value in numerical evaluation at stagnation points or no-slip boundaries, the above formula is modified to

$$m = \frac{h}{a^2 + 2h}.$$

This modified formula is used everywhere in the flowfield. The apparent indeterminacy, which is unique to the curvilinear coordinates, results from requiring the terms in the square bracket in Eq. (15d) to form a perfect square; other formulations may not have this problem. It is noted that, since $\lim_{u\to 0, v\to 0} u_\xi^2/(u^2+v^2)$ has a finite value, the above indeterminacy occurs only in the numerical evaluation but not in the continuous form; therefore, it does not represent a deficiency in the Van Leer splitting theory. The concentration fluxes simply follow from a linear convection principle; i.e.,

$$\tilde{\mathbf{F}}_5^{\pm} = \frac{C_1}{\rho}\tilde{\mathbf{F}}_1^{\pm}, \tag{15e}$$

$$\tilde{\mathbf{F}}_6^{\pm} = \frac{C_2}{\rho}\tilde{\mathbf{F}}_1^{\pm}, \tag{15f}$$

$$\tilde{\mathbf{F}}_7^{\pm} = \frac{C_3}{\rho}\tilde{\mathbf{F}}_1^{\pm}, \tag{15g}$$

$$\tilde{\mathbf{F}}_8^{\pm} = \frac{C_4}{\rho}\tilde{\mathbf{F}}_1^{\pm}. \tag{15h}$$

The split fluxes in η-direction can be similarly obtained.

3.3. *Evaluation of Viscous Fluxes*

The viscous flux vector in general coordinates is expressed as the inner product of the cell surface unit vector and the Cartesian components of the flux vector, which results in

$$\tilde{\mathbf{F}}_v = \frac{1}{\sqrt{x_\eta^2 + y_\eta^2}}\begin{pmatrix} 0 \\ y_\eta\tau_{xx} - x_\eta\tau_{xy} \\ y_\eta\tau_{xy} - x_\eta\tau_{yy} \\ y_\eta\Omega_x - x_\eta\Omega_y \\ -C_1(y_\eta\tilde{u}_1 - x_\eta\tilde{v}_1) \\ -C_2(y_\eta\tilde{u}_2 - x_\eta\tilde{v}_2) \\ -C_3(y_\eta\tilde{u}_3 - x_\eta\tilde{v}_3) \\ -C_4(y_\eta\tilde{u}_4 - x_\eta\tilde{v}_4) \end{pmatrix}, \tag{16}$$

where, as in the case of inviscid fluxes, the metrics are evaluated at the cell interface. The form for $\tilde{\mathbf{G}}_v$ is obtained simply by replacing metrics y_η and x_η with $-y_\xi$ and $-x_\xi$, respectively. The evaluation of the terms in Eq. (16) amounts to calculating the Cartesian gradients at the cell interfaces. This requires the construction of an auxiliary cell whose two sides in the ξ-direction contain the center of the two neighboring regular cells. In the equations presented in this and the following sections, the integer indices i, j denote the cell-center location, and the half-integer indices denotes the location of the cell interface. The Cartesian gradients for a generic function f at the regular cell interface $i+\frac{1}{2}$ are then evaluated by

$$\left(\frac{\partial f}{\partial x}\right)_{i+1/2,j} = [y_{\eta+1/2,j}(f_{i+1,j} - f_{i,j}) - y_{\xi_{i+1/2,j}}(f_{i+1/2,j+1/2} - f_{i+1/2,j-1/2})]/V_{i+1/2,j}, \tag{17a}$$

$$\left(\frac{\partial f}{\partial y}\right)_{i+1/2,j} = [x_{\xi_{i+1/2,j}}(f_{i+1/2,j+1/2} - f_{i+1/2,j-1/2}) - x_{\eta_{i+1/2,j}}(f_{i+1,j} - f_{i,j})]/V_{i+1/2,j}, \tag{17b}$$

where $V_{i+1/2,j}$ is the volume of the auxiliary cell, and

$$x_{\eta_{i+1/2,j}} = x_{i+1/2,j+1/2} - x_{i+1/2,j-1/2}$$
$$y_{\eta_{i+1/2,j}} = y_{i+1/2,j+1/2} - y_{i+1/2,j-1/2}$$
$$x_{\xi_{i+1/2,j}} = x_{i+1,j} - x_{i,j}$$
$$y_{\xi_{i+1/2,j}} = y_{i+1,j} - y_{i,j}.$$

The variables f with half-integer indices are not available from the solution of the governing equations, and thus need to be approximated. The average of the four adjacent cell-center values is adopted here.

3.4. *Spatial Differencing*

A cell-centered finite-volume formulation is adopted for the spatial differencing. This amounts to integrating the governing equations via Green's theorem and evaluating the fluxes at each interface. The discretized form of the explicit operator (residual) in two dimensions is given as

$$\begin{aligned}\mathbf{R} = &(\sqrt{x_\eta^2 + y_\eta^2}\,(\tilde{\mathbf{F}} - \tilde{\mathbf{F}}_v))_{i+1/2,j} \\ &- (\sqrt{x_\eta^2 + y_\eta^2}\,(\tilde{\mathbf{F}} - \tilde{\mathbf{F}}_v))_{i-1/2,j} \\ &+ (\sqrt{x_\xi^2 + y_\xi^2}\,(\tilde{\mathbf{G}} - \tilde{\mathbf{G}}_v))_{i,j+1/2} \\ &- (\sqrt{x_\xi^2 + y_\xi^2}\,(\tilde{\mathbf{G}} - \tilde{\mathbf{G}}_v))_{i,j-1/2} - \mathbf{S}_{i,j} V_{i,j}, \end{aligned} \tag{18}$$

where $V_{i,j}$ is the cell volume, $(\sqrt{x_\eta^2 + y_\eta^2})_{i\pm 1/2,j}$ and $(\sqrt{x_\xi^2 + y_\xi^2})_{i,j\pm 1/2}$ are the cell interface areas (lengths in 2D). The coordinates of the cell center is defined by averaging the four corners, and the cell volume is given by the expression

$$\begin{aligned} V_{i,j} = 0.5[&(x_{i+1/2,j+1/2} - x_{i-1/2,j-1/2}) \\ &\cdot (y_{i-1/2,j+1/2} - y_{i+1/2,j-1/2}) \\ &- (x_{i-1/2,j+1/2} - x_{i+1/2,j-1/2}) \\ &\cdot (y_{i+1/2,j+1/2} - y_{i-1/2,j-1/2})]. \end{aligned}$$

The viscous fluxes are evaluated by central differencing, while the inviscid fluxes are treated by a second-order upwind method. The upwind method is constructed by first splitting the local interface inviscid flux into positive and negative components, according to the wave propagation directions, as follows, for the flux in the ξ-direction (omitting the index j):

$$\tilde{\mathbf{F}}_{i+1/2} = \tilde{\mathbf{F}}^+_{i+1/2} + \tilde{\mathbf{F}}^-_{i+1/2}. \tag{19a}$$

The cell-interface fluxes are then determined by interpolation from the cell-center values:

$$\tilde{\mathbf{F}}^+_{i+1/2} = \tilde{\mathbf{F}}^+_i + \alpha_i \Delta_\xi^- \tilde{\mathbf{F}}^+_i, \tag{19b}$$

$$\tilde{\mathbf{F}}^-_{i+1/2} = \tilde{\mathbf{F}}^-_{i+1} - \beta_i \Delta_\xi^+ \tilde{\mathbf{F}}^-_{i+1}, \tag{19c}$$

where

$$\alpha_i = \frac{l_i}{l_{i-1} + l_i}, \qquad \beta_i = \frac{l_{i+1}}{l_{i+1} + l_{i+2}},$$

$$l_i = 0.5\,[(\sqrt{x_\xi^2 + y_\xi^2})_{i,j+1/2} + (\sqrt{x_\xi^2 + y_\xi^2})_{i,j-1/2}],$$

and Δ_ξ^- and Δ_ξ^+ are the backward and forward difference operators, respectively, in the ξ-direction, and l_i is the width of cell (i,j) in the ξ-direction. Combining "+" and "−" fluxes, the interface flux is obtained as

$$\begin{aligned}\tilde{\mathbf{F}}_{i+1/2} = &\tfrac{1}{2}(\tilde{\mathbf{F}}_i + \tilde{\mathbf{F}}_{i+1}) - \tfrac{1}{2}\Delta_\xi^+(\tilde{\mathbf{F}}^+_i - \tilde{\mathbf{F}}^-_\xi) \\ &+ (\alpha_i \Delta_\xi^- \tilde{\mathbf{F}}^+_i - \beta_i \Delta_\xi^+ \tilde{\mathbf{F}}^-_{i+1}). \end{aligned} \tag{20}$$

The first term is a simple average of the cell-center fluxes, while the combination of the first and second terms constitutes the first-order upwind scheme. The third term represents the anti-diffusive flux which makes the scheme second-order accurate. The flux differences appearing in Eqs. (19) and (20) can be evaluated using either a flux-vector splitting scheme or a flux-difference splitting scheme. Both schemes, i.e., the Van Leer's flux-vector splitting and the Roe's flux-difference splitting, are considered in the paper.

Note that the nonuniformity of cell sizes is taken into account in α_i and β_i. Improvements of accuracy were reported in [25] by properly accounting for the cell nonuniformity, which can contribute to large errors in regions of highly stretched grids. To eliminate oscillations and to obtain a sharp representation of discontinuities, we use an upwind-based TVD scheme, which amounts to introducing limiters in the higher-order terms in Eq. (19):

$$\tilde{\mathbf{F}}^+_{i+1/2} = \tilde{\mathbf{F}}^+_i + \alpha_i \Psi^+_i \Delta_\xi^- \tilde{\mathbf{F}}^+_i, \tag{21a}$$

$$\tilde{\mathbf{F}}^-_{i+1/2} = \tilde{\mathbf{F}}^-_{i+1} - \beta_i \Psi^-_{i+1} \Delta_\xi^+ \tilde{\mathbf{F}}^-_{i+1}. \tag{21b}$$

The limiters Ψ^+ and Ψ^- are nonlinear functions of some approximate ratio of neighboring flux differences. A "min-mod" type limiter function is used in the present study; more details regarding the present TVD formulation can be found in [15, 26].

In Eqs. (20) and (21), the "+" and "−" fluxes, $\tilde{\mathbf{F}}^\pm$, are first obtained at cell centers. Their values at cell interfaces are then determined by upwind extrapolations. This is commonly referred to as a flux differencing approach [27]. In multi-dimensional curvilinear coordinates the flux differencing approach is cumbersome to implement, as the choice of metrics for the higher-order terms in the normal fluxes can be ambiguous in regions of highly convoluted grids.

To circumvent the difficulty of metric ambiguity, the MUSCL approach [27] is adopted (for the Van Leer splitting) in the present study. In MUSCL, one extrapolates cell-center values of flow variables $\mathbf{Q}$ toward the interfaces (metric factors are not involved) and then obtains the interface split fluxes using the extrapolated variables, i.e.,

$$\tilde{\mathbf{F}}^+_{i+1/2} = \tilde{\mathbf{F}}^+(\mathbf{Q}^-_{i+1/2}), \tag{22a}$$

$$\tilde{\mathbf{F}}^-_{i+1/2} = \tilde{\mathbf{F}}^-(\mathbf{Q}^+_{i+1/2}), \tag{22b}$$

where the interface flow variables $\mathbf{Q}^{\pm}$ are defined as

$$\mathbf{Q}^{-}_{i+1/2} = \mathbf{Q}_i + \frac{l_i}{2}\Phi^{-}_{i+1/2}, \tag{23a}$$

$$\mathbf{Q}^{+}_{i+1/2} = \mathbf{Q}_{i+1} - \frac{l_{i+1}}{2}\Phi^{+}_{i+1/2}, \tag{23b}$$

and flux limiting is applied through $\Phi^{\pm}$,

$$\Phi^{+}_{i+1/2} = \max[0, \min(\Delta_{+_i} \operatorname{sgn} \Delta_{-_i}, b\Delta_{-_i} \operatorname{sgn} \Delta_{+_i})] \operatorname{sgn} \Delta_{+_i}, \tag{24a}$$

$$\Phi^{-}_{i+1/2} = \max[0, \min(\Delta_{-_i} \operatorname{sgn} \Delta_{+_i}, b\Delta_{+_i} \operatorname{sgn} \Delta_{-_i})] \operatorname{sgn} \Delta_{-_i}, \tag{24b}$$

where

$$\Delta_{+_i} \equiv \frac{2(\mathbf{Q}_{i+1} - \mathbf{Q}_i)}{(l_i + l_{i+1})}, \tag{25a}$$

$$\Delta_{-_i} \equiv \frac{2(\mathbf{Q}_i - \mathbf{Q}_{i-1})}{(l_{i-1} + l_i)}, \tag{25b}$$

$$b = 1. \tag{25c}$$

Conservative variables are used for $\mathbf{Q}$ in Ref. [27], however, it was found that using primitive variables, i.e., $\mathbf{Q} = (\rho, u, v, p, C_i/\rho)$, yields better convergence for flows with strong shocks, as was also found in Ref. [28]. Primitive variables are used in the present study. It is also noted that cell-length weighting for nonuniform grid spacing is included in Eqs. (23)–(25) in the present formulation.

The derivation of the split fluxes in the η-direction follows the same procedure as described in Eqs. (19)–(25).

4. LU IMPLICIT ALGORITHM

The discretized governing equations may be solved using either an explicit or implicit scheme. When only steady-state solutions are required, the implicit scheme is generally favored for its superior convergence. Since the mid-seventies, the ADI method has been successfully applied to various aerodynamic problems involving calorically perfect gases. Since the ADI method (and most other implicit schemes) requires inversion of block banded (tridiagonal or pentadiagonal) matrices, it becomes prohibitively inefficient for chemical/thermal nonequilibrium flows due to the large block size resulting from the large number of species and thermal energy equations. One alternative is to use the lower–upper (LU) approximation to factor the implicit operator [3, 5, 18, 19]. Unlike the block banded system of the ADI scheme, the LU scheme results in a block diagonal system for which the computational inversion effort is moderate. Furthermore, the LU factors are fully vectorizable, providing additional advantage in numerical efficiency. In the following, we first present the construction of the flux and chemical source Jacobian matrices for chemical nonequilibrium gases, and then we show the implementation of the LU algorithm and discuss the advantages of the method.

4.1. *Split-Flux Jacobian Matrices*

For a gas with an arbitrary equation of state, the flux vectors $\mathbf{F}(\mathbf{U})$ and $\mathbf{G}(\mathbf{U})$ are not homogeneous functions of degree one in $\mathbf{U}$. In this case, the inviscid flux $\mathbf{F}$ (similarly for $\mathbf{G}$) can be expressed as the sum of a homogeneous flux $\mathbf{F}_h$ and an inhomogeneous flux $\mathbf{F}_{in}$, i.e.,

$$\mathbf{F} = \mathbf{F}_h + \mathbf{F}_{in}, \tag{26a}$$

and

$$\mathbf{A} = \frac{\partial \mathbf{F}}{\partial \mathbf{U}} = \mathbf{A}_h + \mathbf{A}_{in}; \tag{26b}$$

here $\mathbf{F}_h = \mathbf{A}\mathbf{U}$ and $\mathbf{F} = \mathbf{A}_h\mathbf{U}$, yielding $\mathbf{F}_{in} = -\mathbf{A}_{in}\mathbf{U}$. It was shown in [14, 15] that for a gas, with an arbitrary equation of state, $\mathbf{F}_{in}$ is nonzero and the matrices $\mathbf{A}$ and $\mathbf{A}_h$ have a complete set of eigenvectors, while $\mathbf{A}_{in}$ does not. It is noted that the eigenvalues and eigenvectors of $\mathbf{A}$ and $\mathbf{A}_h$ are generally not the same. Since $\mathbf{A}_{in}$ does not have a complete set of eigenvectors, a system of equations that consists of $\mathbf{F}_{in}$ alone does not have hyperbolic character. In consequence, the inhomogeneous flux and its associated Jacobian $\mathbf{A}_{in}$ do not need splitting. Hence the split fluxes for a gas with arbitrary equation of state may be expressed as

$$\mathbf{F}^{\pm} = \mathbf{F}^{\pm}_h + \tfrac{1}{2}\mathbf{F}_{in}, \quad = (\mathbf{A}^{\pm} - \tfrac{1}{2}\mathbf{A}_{in})\mathbf{U}, \tag{27}$$

and $(\mathbf{A}^{\pm} - \frac{1}{2}\mathbf{A}_{in})$ are the split Jacobian matrices to be used in the implicit operator.

If the equation of state has the functional form

$$p = \rho f(e, Y_{i, i=1,\ldots,N-1}), \tag{28}$$

then it can be shown that $\mathbf{F}_{in} = 0$, $\mathbf{A}_{in} = 0$, and the homogeneous property of the flux vector is recovered. The equation of state used in the present study, i.e., Eq. (3), is clearly a special case of Eq. (28), and therefore $\mathbf{F} = \mathbf{A}\mathbf{U}$; hence the split flux Jacobian derived in Eq. (12) may be used in the implicit operator. We note that metric factors at interfaces are used in $\tilde{\mathbf{A}}^{\pm}$. We further note that the $\tilde{\mathbf{A}}^{\pm}$ of Eq. (12) are the approximate split Jacobians, which

are slightly different from the true split Jacobians, $\mathbf{A}^{\pm}_{\text{true}} = \partial \tilde{\mathbf{F}}^{\pm}/\partial \mathbf{U}$. The use of approximate split Jacobians in the implicit operator may adversely affect the convergence of the scheme. However, since evaluation of the true split Jacobians for a nonequilibrium gas is computationally expensive, no attempt was made to use the true split Jacobian in the present study. Later in the Numerical Test section, we will show that the approximate Jacobians yield good convergence rates for a wide variety of flows.

4.2. *Viscous Flux Jacobian*

Although the full Navier–Stokes equations are considered in the evaluation of the residual operator, for simplicity the thin-layer version of the viscous fluxes is used in the implicit operator. The two-dimensional thin-layer viscous flux vector in general coordinates can be written as

$$\tilde{\mathbf{G}}_v = \begin{bmatrix} 0 \\ \beta_1 \mu \dfrac{\partial u}{\partial \eta} + \beta_2 \mu \dfrac{\partial v}{\partial \eta} \\ \beta_2 \mu \dfrac{\partial u}{\partial \eta} + \beta_3 \mu \dfrac{\partial v}{\partial \eta} \\ \beta_1 \mu u \dfrac{\partial u}{\partial \eta} + \beta_2 \mu \dfrac{\partial uv}{\partial \eta} + \beta_3 \mu v \dfrac{\partial v}{\partial \eta} \\ \quad + \beta_4 \left(k \dfrac{\partial T}{\partial \eta} + \rho \sum_{i=1}^{N} h_i D_{im} \dfrac{\partial Y_i}{\partial \eta} \right) \\ \beta_4 \rho D_{1m} \dfrac{\partial Y_1}{\partial \eta} \\ \beta_4 \rho D_{2m} \dfrac{\partial Y_2}{\partial \eta} \\ \beta_4 \rho D_{3m} \dfrac{\partial Y_3}{\partial \eta} \\ \beta_4 \rho D_{4m} \dfrac{\partial Y_4}{\partial \eta} \end{bmatrix}, \tag{29}$$

where

$$\beta_1 = (\tfrac{4}{3} y_\xi^2 + x_\xi^2)/V, \qquad \beta_2 = -\tfrac{1}{3} x_\xi y_\xi / V,$$

$$\beta_3 = (\tfrac{4}{3} x_\xi^2 + y_\xi^2)/V, \qquad \beta_4 = (x_\xi^2 + y_\xi^2)/V,$$

and V is the cell volume.

Assuming the transport coefficients μ, k, and D_{im} are frozen with respect to changes in $\mathbf{U}$ and space, it can be shown that

$$\frac{\partial \tilde{\mathbf{G}}_v}{\partial \mathbf{U}} = \frac{\partial}{\partial \eta} \frac{\partial \tilde{\mathbf{G}}_v}{\partial (\partial \mathbf{U}/\partial \eta)}.$$

Hence the viscous Jacobian, $\tilde{\mathbf{T}} = \partial \tilde{\mathbf{G}}_v / \partial (\partial \mathbf{U}/\partial \eta)$ is obtained,

$$\tilde{\mathbf{T}} = \begin{bmatrix} 0 & 0 & 0 & 0 & 0 \\ \dfrac{-\mu}{\rho}(\beta_1 u + \beta_2 v) & \beta_1 \dfrac{\mu}{\rho} & \beta_2 \dfrac{\mu}{\rho} & 0 & 0 \\ \dfrac{-\mu}{\rho}(\beta_2 u + \beta_3 v) & \beta_3 \dfrac{\mu}{\rho} & \beta_2 \dfrac{\mu}{\rho} & 0 & 0 \\ \Theta & \dfrac{\mu}{\rho}(\beta_1 u + \beta_2 v) & \dfrac{\mu}{\rho}(\beta_2 u + \beta_3 v) & 0 & 0 \\ & -\beta_4 \dfrac{k}{\rho C_v} u & -\beta_4 \dfrac{k}{\rho C_v} v & 0 & 0 \\ -\beta_4 D_{1m} Y_1 & 0 & 0 & 0 & 0 \\ -\beta_4 D_{2m} Y_2 & 0 & 0 & 0 & 0 \\ -\beta_4 D_{3m} Y_3 & 0 & 0 & 0 & 0 \\ -\beta_4 D_{4m} Y_1 & 0 & 0 & 0 & 0 \end{bmatrix}$$

$$\begin{bmatrix} 0 & 0 & 0 & 0 & 0 \\ 0 & 0 & 0 & 0 & 0 \\ 0 & 0 & 0 & 0 & 0 \\ \beta_4 \dfrac{k}{\rho C_v} & \alpha_1 & \alpha_2 & \alpha_3 & \alpha_4 \\ 0 & \beta_4 D_{1m} & 0 & 0 & 0 \\ 0 & 0 & \beta_4 D_{2m} & 0 & 0 \\ 0 & 0 & 0 & \beta_4 D_{3m} & 0 \\ 0 & 0 & 0 & 0 & \beta_4 D_{4m} \end{bmatrix}, \tag{30}$$

where

$$\Theta = -\frac{\mu}{\rho}(\beta_1 u^2 + \beta_3 v^2 + 2\beta_2 uv) + \beta_4 \left[\frac{k}{\rho C_v} \left(-e + \frac{u^2 + v^2}{2} \right) - \sum_{i=1}^{N-1} Y_i \left(\bar{h}_i D_{im} - \frac{k}{\rho C_v} \bar{e}_i \right) \right],$$

$$\alpha_i = \beta_4 \left(\bar{h}_i D_i - \frac{k}{\rho C_v} \bar{e}_i \right),$$

$$\bar{h}_i = h_i - h_N, \qquad \bar{e}_i = e_i - e_N,$$

$$C_v = \sum_{i=1}^{N} Y_i C_{v_i},$$

and C_{v_i} is the constant volume specific heat of species i.

4.3. *Chemical Source Term and Source Jacobian*

For a set of N_R elementary reactions involving N species, the rate equations can be written in the general form

$$\sum_{j=1}^{N} \nu'_{ij} n_j \underset{k_{b_i}}{\overset{k_{f_i}}{\rightleftarrows}} \sum_{j=1}^{N} \nu''_{ij} n_j, \quad i = 1, 2, ..., N_R, \tag{31}$$

where ν'_{ij} and ν''_{ij} are the stoichiometric coefficients for species j appearing as a reactant in the ith forward and backward reactions, respectively, and n_j is the molar concentration for species j ($n_j = C_j/W_j$). Also, k_{f_i} and k_{b_i} respectively are the forward and backward reaction rate constants for the ith reaction step. The reaction rate constant k_i (k_{f_i} or k_{b_i}) is given empirically by the Arrhenius expression

$$k_i = A_i T^{m_i} e^{-E_i/R_u T}, \tag{32}$$

where E_i represents the activation energy, and A_i and m_i are constants.

From Eq. (31) the rate of change of mass concentration of species j is obtained by summing up the changes due to all reaction steps,

$$S_j = W_j \sum_{i=1}^{N_R} \left[(\nu''_{ij} - \nu'_{ij}) \times \left(k_{f_i} \prod_{l=1}^{N} n_l^{\nu'_{il}} - k_{b_i} \prod_{l=1}^{N} n_l^{\nu''_{il}} \right) \right]. \tag{33}$$

We observe from Eqs. (32) and (33) that the chemical source term is an exponential function of temperature and a nonlinear function of species concentration. Because of the highly nonlinear nature of chemical kinetics and the vastly different chemical time scales involved in the individual elementary reactions, the set of species equations in Eq. (1) is generally very stiff. To mitigate the stiffness problem, the chemical source terms are treated implicitly so that the stiffness of the species equations does not appreciably degrade the rate of convergence or upset the numerical stability. Details for the construction of the source term Jacobian can be found in [15].

We note that, despite the implicit treatment of chemical source terms, the set of species equations still becomes very difficult to solve numerically at regions where the temperature and density are very high and chemical reactions are intensive. In fact, we have observed throughout the study that the maximum CFL number allowable for stable computation is very often limited by chemical kinetics (the maximum CFL number for nonequilibrium calculations is limited to between 2 and 10, depending on the field temperature and shock strength), and the benefit of large CFL number (CFL $\gg 1$) associated with implicit schemes for ideal-gas flows is not fully realized in nonequilibrium computations in the present study. But the advantage over explicit methods for the same problem is still very great. This issue will be further discussed in the Convergence Property section.

4.4. *LU Factorization*

Discretizing the implicit operator using first-order upwind differencing for inviscid terms and central-differencing for viscous terms, the governing equations in the finite-volume form can be written as

$$\{\mathbf{I} + \Delta t[\Delta_\xi^- \tilde{\mathbf{A}}_{i,j}^+ + \Delta_\xi^+ \tilde{\mathbf{A}}_{i,j}^- + \Delta_\eta^- \tilde{\mathbf{B}}_{i,j}^+ + \Delta_\eta^+ \tilde{\mathbf{B}}_{i,j}^- - (\tilde{\mathbf{T}}_{i,j+1} - 2\tilde{\mathbf{T}}_{i,j} + \tilde{\mathbf{T}}_{i,j-1}) - \mathbf{H}_{i,j}]\}\, \delta\tilde{\mathbf{U}} = -\Delta t\, \mathbf{R}_{i,j}, \tag{34}$$

where $\mathbf{H} = \partial \mathbf{S}/\partial \mathbf{U}$ is the chemical source term Jacobian [15], $\tilde{\mathbf{T}}$ is the viscous Jacobian as defined in Eq. (30), $\mathbf{R}_{i,j}$ is obtained by Eq. (18), $\delta\tilde{\mathbf{U}} = V\,\delta\mathbf{U}$, and V is the cell volume. Substituting the one-sided spatial differencing formula for $\Delta^{\pm}$, Eq. (34) becomes

$$[\mathbf{I} + \Delta t\,(\tilde{\mathbf{A}}_{i,j}^+ - \tilde{\mathbf{A}}_{i,j}^- + \tilde{\mathbf{B}}_{i,j}^+ - \tilde{\mathbf{B}}_{i,j}^- + 2\tilde{\mathbf{T}}_{i,j} - \mathbf{H}_{i,j}) - \Delta t\,(\tilde{\mathbf{A}}_{i-1,j}^+ + \tilde{\mathbf{B}}_{i,j-1}^+ + \tilde{\mathbf{T}}_{i,j-1}) + \Delta t\,(\tilde{\mathbf{A}}_{i+1,j}^- + \tilde{\mathbf{B}}_{i,j+1}^- - \tilde{\mathbf{T}}_{i,j+1})]\, \delta\tilde{\mathbf{U}} = -\Delta t\, \mathbf{R}_{i,j}. \tag{35}$$

Equation (35) can be symbolically expressed as

$$[D + L + U]\, \delta\tilde{\mathbf{U}} = -\Delta t\, \mathbf{R}, \tag{36}$$

where

$$\begin{aligned} D &= \mathbf{I} + \Delta t\,(\tilde{\mathbf{A}}_{i,j}^+ - \tilde{\mathbf{A}}_{i,j}^- + \tilde{\mathbf{B}}_{i,j}^+ - \tilde{\mathbf{B}}_{i,j}^- + 2\tilde{\mathbf{T}}_{i,j} - \mathbf{H}_{i,j}), \\ L &= -\Delta t\,(\tilde{\mathbf{A}}_{i-1,j}^+ + \tilde{\mathbf{B}}_{i,j-1}^+ + \tilde{\mathbf{T}}_{i,j-1}), \\ U &= \Delta t\,(\tilde{\mathbf{A}}_{i+1,j}^- + \tilde{\mathbf{B}}_{i,j+1}^- - \tilde{\mathbf{T}}_{i,j+1}). \end{aligned} \tag{37}$$

Note that D consists of only diagonal terms, L only the terms in the lower triangular matrix, and U the upper triangular matrix. The left-hand side of Eq. (36) can be approximately factored into the product of two operators

$$(D + L)\, D^{-1} (D + U)\, \delta\tilde{\mathbf{U}} = -\Delta t\, \mathbf{R}. \tag{38}$$

This scheme can be implemented in the following sequence:

$$(D + L)\, \delta\tilde{\mathbf{U}}^* = -\Delta t\, \mathbf{R}, \tag{39a}$$

$$(D + U)\, \delta\tilde{\mathbf{U}} = D\, \delta\tilde{\mathbf{U}}^*, \tag{39b}$$

$$\tilde{\mathbf{U}}^{n+1} = \tilde{\mathbf{U}}^n + \delta\tilde{\mathbf{U}}. \tag{39c}$$

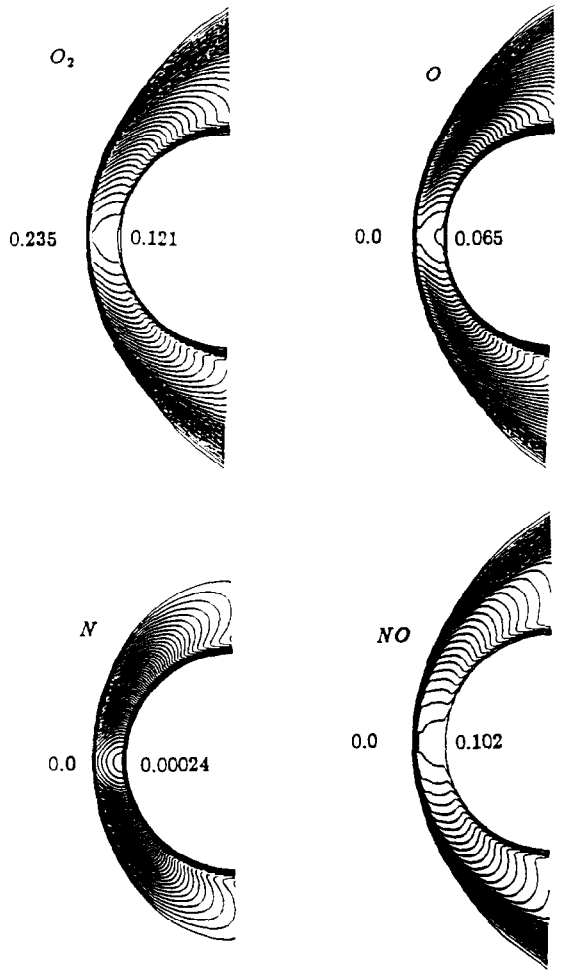

FIG. 2. Species mass fraction contours for flow over a half-cylinder, $M_\infty = 7.0$.

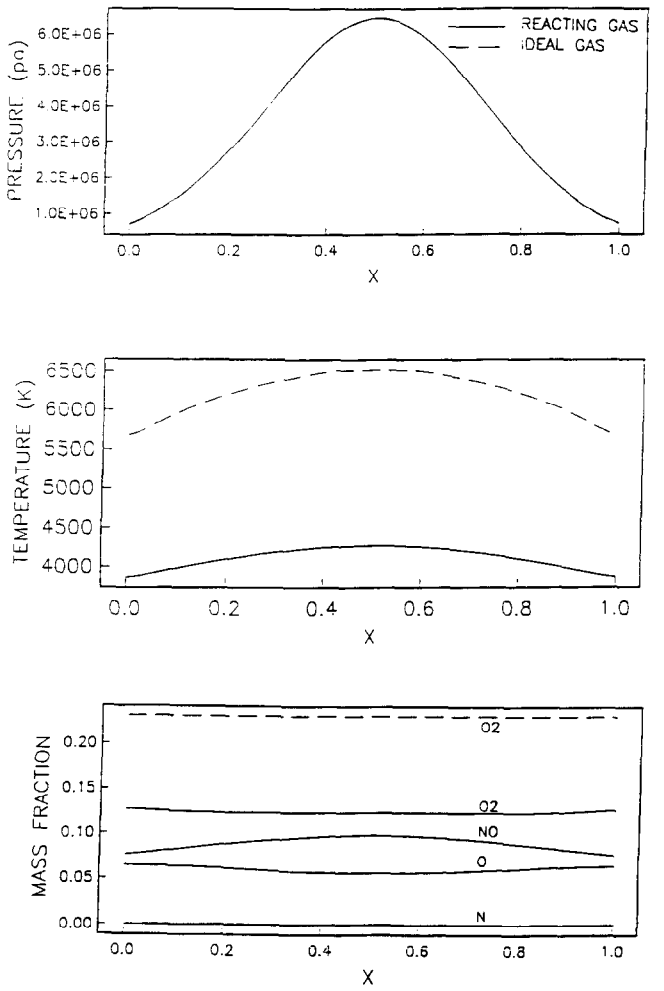

FIG. 3. Wall pressure, temperature, and species mass fraction profiles for flow over a half-cylinder, $M_\infty = 7.0$.

model would obtain (see Fig. 3). The lower temperatures are obviously the result of air dissociation (see Fig. 2) and the increased specific heat at high temperatures.

It should be mentioned here that the Roe flux-difference splitting was also used to calculate this flow, and the results (not shown here) showed the presence of an expansion shock as the flow reaccelerates from near the stagnation point to supersonic velocity farther downstream along the cylinder wall. This result is not surprising, however, since it is well known that Roe splitting violates the entropy condition and admits expansion shocks [7]. Although adding a small amount of dissipation near the sonic point may circumvent this difficulty, no such attempt was made in the present study.

Figure 2 shows the mass fraction contours for species O_2, O, NO, and N, with their maximum and minimum values indicated. Along the symmetry plane (the plane through the stagnation point), the temperature and density increases across the bow shock are the largest, resulting in very intensive chemical reactions behind the shock, as indicated by the rapid changes of mass fraction in this region. Far away from the symmetry plane, the increases in temperature and density are smaller, and therefore chemical reactions are proceeding at a slower rate, resulting in a more gradual change of species concentrations.

Figure 3 shows the pressure, temperature, and mass fraction profiles along the cylinder wall. The abscissa **X** of the coordinates denotes the position along the half-cylinder wall, from bottom to top. Both the ideal- and nonequilibrium-gas results are presented for comparison. The ideal-gas model (with $\gamma = 1.365$ for air at $T = 600$ K, $p = 1$ atm) yields higher temperatures than the nonequilibrium model, while the two models produce almost exactly the same pressures. The mass fraction profiles indicate that significant dissociation and recombination reactions occur and the ideal-gas model fails to represent the flowfield. It is also observed that, because of the high pressure and temperature levels and the long flow residence

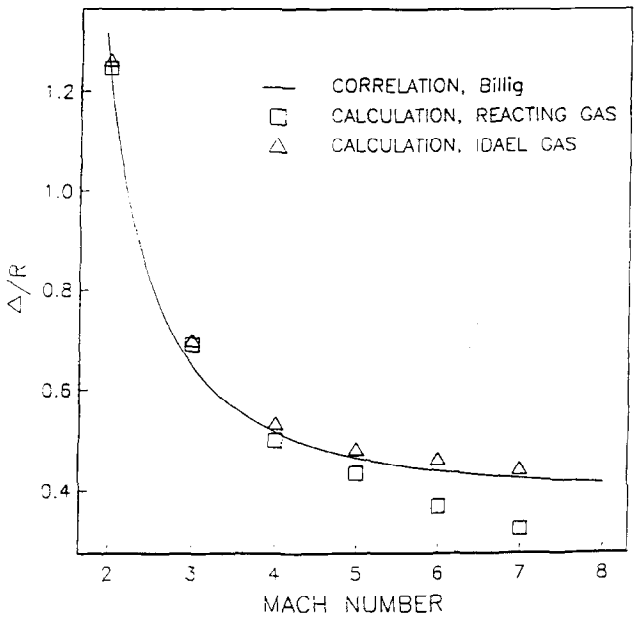

FIG. 4. Shock standoff distance for flow over a half-cylinder.

time (due to the low velocity in the boundary layer) near the wall, the mass fractions predicted by the nonequilibrium

Ambrosio and Wortman [29] correlated the experimental data for shock standoff distance from a circular-cylinder over a wide range of Mach numbers. In Fig. 4, we compare the present numerical results of the normalized standoff distance Δ/R (R is the radius of cylinder) with the correlation in [29]. Since the experimental data adopted in [29] were based on tests made at relatively low total temperatures, it would be expected that the correlation would be most accurate for an ideal gas with $\gamma = 1.4$; hence, in addition to the real-gas predictions, we also present results of ideal-gas calculations (with $\gamma = 1.4$). Figure 4 shows that the ideal-gas predictions agree very well with the correlation in [29], while the real-gas calculations yield reduced standoff distance at higher Mach numbers, in accordance with the finding by Billig [30]. The real-gas effect of reduction in standoff distance at high Mach numbers can be attributed to the stronger compression (larger density jump across the shock) in real gases, caused by the much reduced temperature rise behind the shock. At lower Mach numbers, chemical reactions and real-gas effects are not significant due to the smaller temperature rise across the shock. Consequently, the nonequilibrium model yields similar shock standoff distance as the ideal-gas model.

5.2. *Ramped-Duct Flow*

The adoption of the ramped-duct flow as a model problem is to demonstrate the ability of the present numerical method to resolve the complicated wave structure and flow separation involved in the shock wave/shock wave and shock wave/boundary layer interaction processes. The test model consists of a two-dimensional channel with an 18° compression ramp in front and a 12° expansion ramp in the rear. The inflow pressure is at 1 atm, temperature 500 K, and Mach number 4. The Reynolds number based on the channel height at inlet and freestream velocity is 3.10×10^6. Both Roe and Van Leer splitting are used in this calcula-

differencing) are shown here.

Figure 5 displays the static pressure contours for both the inviscid and viscous calculations. The inviscid result shows that the shock waves are captured very crisply and monotonically. In the viscous case, the flow structure is more complicated, involving the shock wave/shock wave and shock wave/boudary layer interactions and large scale flow separations. The chemical reactions and real-gas effects are not significant in this case due to the relatively low total temperature. In fact, most chemical reactions occur in the near wall region in the viscous case, generating only trace amounts of NO and O species there.

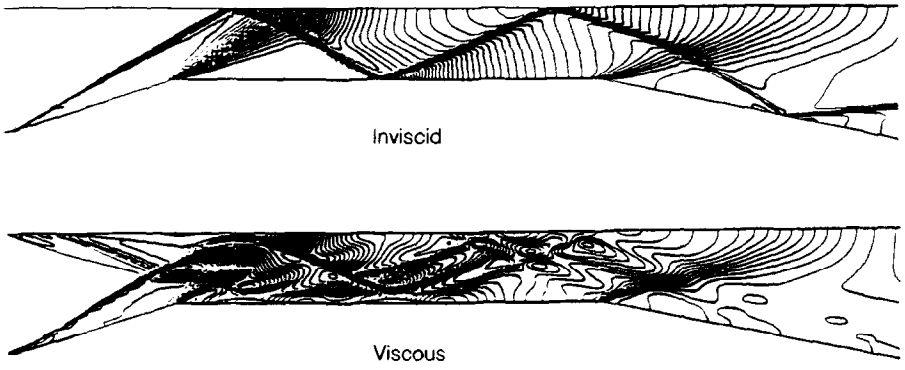

FIG. 5. Static pressure contours for flow in a ramped-duct, $M_\infty = 4.0$.

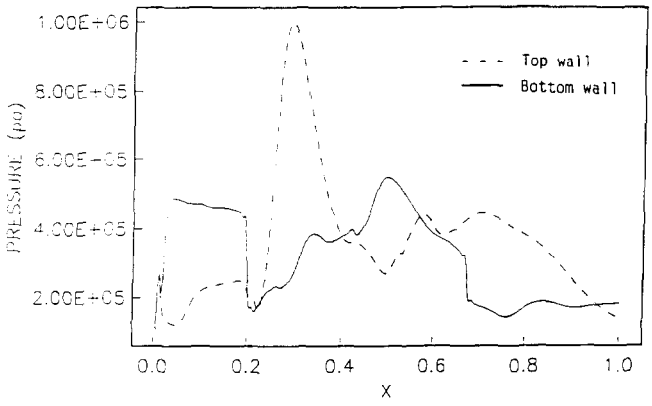

FIG. 6. Wall pressure profiles for flow in a ramped-duct, $M_\infty = 4.0$.

Figure 6 presents the static pressures along the top and bottom walls for the viscous case. The pressure profiles vividly illustrate the various waves, with each pressure peak and valley corresponding to a particular wave action, i.e., the leading edge shock, the ramp shock, the corner expansion wave, the separation shock, the expansion wave behind the crest of the separation bubble, and the reattachment shock. Figure 7 displays the velocity vectors in the duct. For clarity of presentation, only the velocity vector for every three grid points in the streamwise direction and every two grid points in the normal direction is plotted. Two separation zones along the bottom wall and three zones along the top wall can be identified from the vector plot. A close comparison of Figs. 6 and 7 clearly shows the relationship and interactions between the waves and the separation bubbles; in particular, each flow reattachment point corresponds to a strong pressure peak.

5.3. *Shock Wave/Laminar Boundary Layer Interaction*

This test case is adopted to investigate the solution accuracy of the viscous part of the Navier–Stokes equations. The shock wave/laminar boundary layer interaction problem has been studied by several other researchers [31, 32], and a more detailed description of the flow can be obtained from their work. The model problem consists of an oblique shock wave impinging on a flat plate in a supersonic laminar flow. The shock angle is set to 32.6°, the freestream Mach number is 2, and the Reynolds number based on the distance from the flat plate leading edge to the shock impingement point is 0.296×10^6 (the impingement point is not well-defined in viscous flow, and therefore the inviscid impingement point is used for Reynolds number evaluation, see Ref. [31]). The real-gas effects are neglected in this case. The computational domain begins five grid points ahead of the plate, and the top boundary extends far enough so that the leading edge shock and the reflected shock pass through the outflow boundary.

The calculated pressure (p/p_∞) and skin friction coefficient ($C_f = 2\tau_w/\rho_\infty u_\infty^2$, τ_w is the wall shear stress) distributions are shown in Figs. (8a) and (8b), respectively, along with experimental data [33] and numerical results by other researchers [31, 32]. The abscissa **X/L** is the distance from the leading edge of the flat plate, normalized by the length from the leading edge to the shock impingement point. The agreement in wall pressure is very good, but relatively large discrepancy exists between the experimental data and the predictions in skin friction, probably due to the transition from laminar to turbulent flow in the boundary layer downstream of the interaction region, which is not considered in the numerical simulations.

5.4. *Divergent Nozzle Flow*

To further illustrate the nonequilibrium effect, results for air flow with high inlet temperature and pressure, i.e., $T = 5000$ K and $p = 10$ atm, expanding through a divergent nozzle of area-ratio 21 are presented in this subsection. The inflow air upstream of the nozzle entrance is assumed to be at chemical equilibrium with a uniform velocity profile at Mach number of 1.01. The results presented here are obtained using Roe's splitting.

The cross-sectional area (in the unit of m^2/m-width) of the two-dimensional nozzle is given by the equation

$$A(X) = 0.22 + 0.20 \sin\left[\left(\frac{X}{XL} - 0.5\right)\pi + \theta\right],$$

where $XL = 1.5$ m is the nozzle length, $\theta = 0.005$ radians is a small phase angle, and X is the streamwise distance from the inflow plane.

Figure 9 presents the static pressure, temperature, and species mass fractions for O_2, O, N, and NO along the

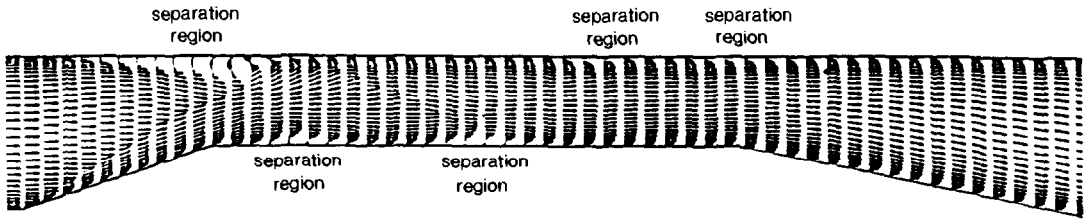

FIG. 7. Velocity vectors for flow in a ramped-duct, $M_\infty = 4.0$.

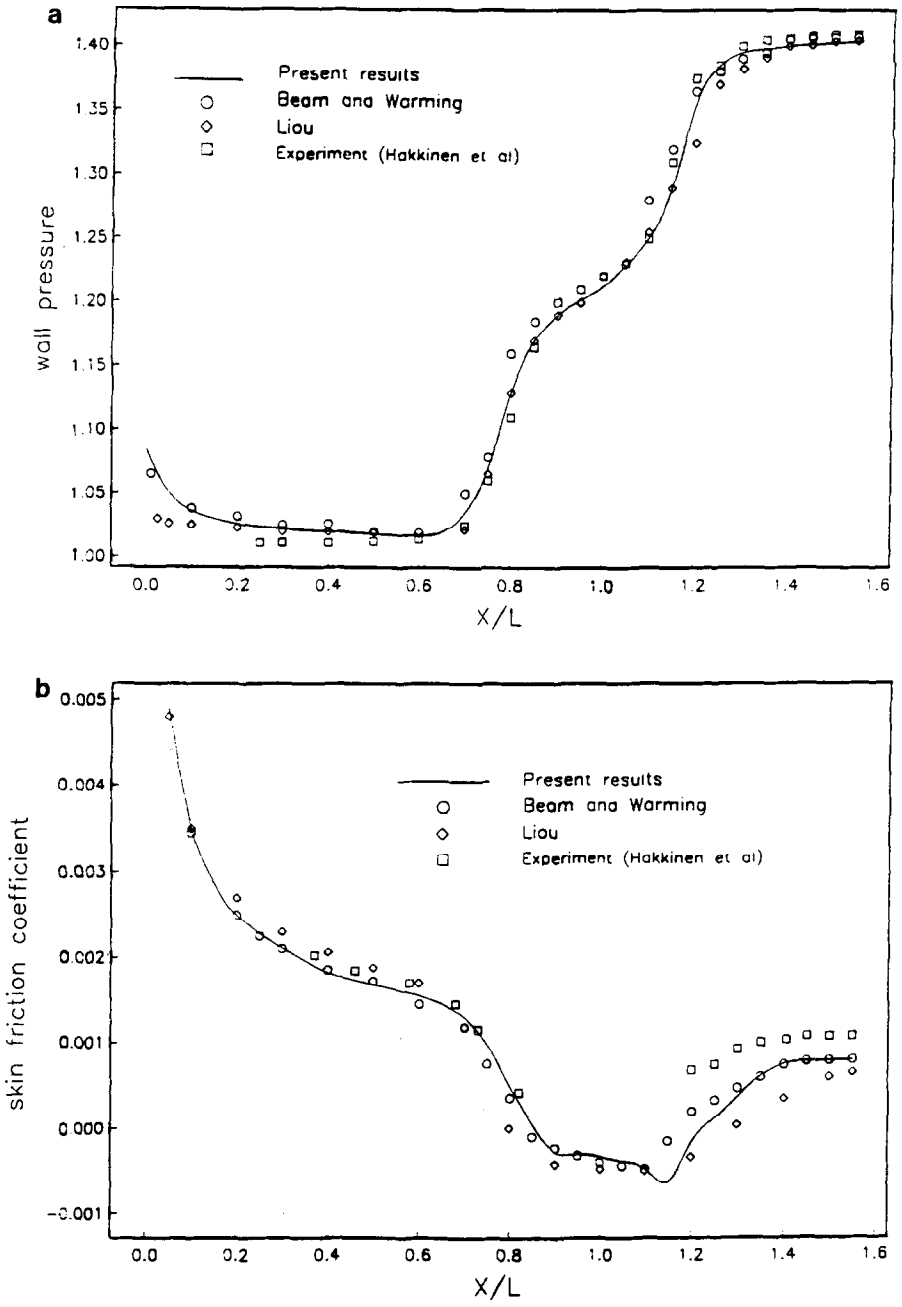

FIG. 8. Comparison of surface pressure and skin friction coefficient for shock/boundary layer interaction problem, $M_\infty = 2.0$, $\mathrm{Re} = 0.296 \times 10^6$: (a) surface pressure distribution; (b) skin friction coefficient distribution.

nozzle centerline. Because of the high temperature and pressure involved, very intensive chemical reactions occur in the front section of the nozzle and species mass fractions change significantly from their initial equilibrium values. But, because of the rapid decrease of temperature and pressure due to the large expansion ratio of the nozzle, chemical reactions become nearly frozen towards the rear section of the nozzle, as depicted in the mass fraction profiles. To illustrate the effects of real-gas property and nonequilibrium chemistry, pressures and temperatures from the frozen-chemistry (allowing specific heat to vary with temperature) and ideal-gas (constant specific heat, $\gamma = 1.4$) calculations are also presented in this figure for comparison. As the air expands through the nozzle, the decrease in temperature and pressure causes the dissociated species (O, N, and NO) to recombine to form O_2 and N_2. In the process of recombination, chemical energy is converted to thermal energy which would slow down the decrease of temperature and

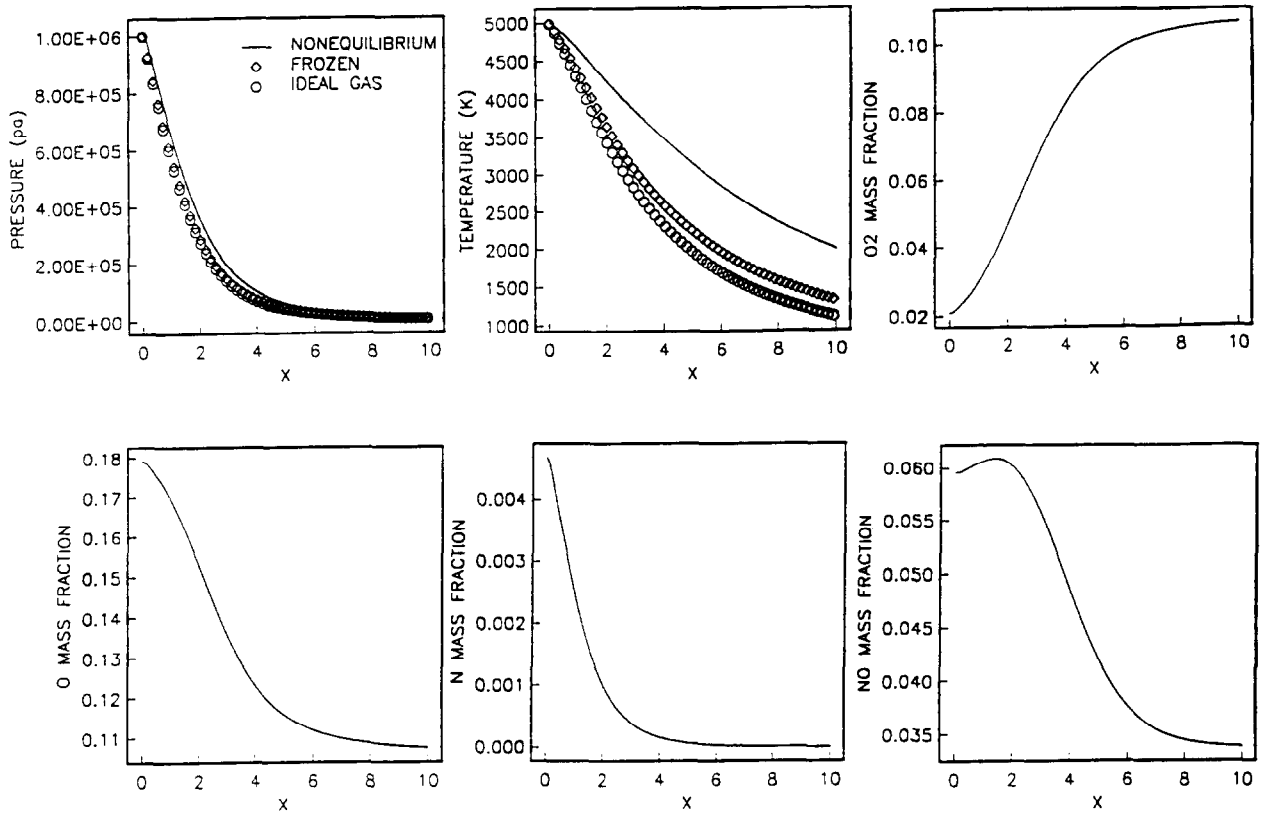

FIG. 9. Pressure, temperature, and species mass fraction profiles along the centerline of the divergent nozzle.

pressure. Since the frozen and ideal-gas models do not account for the recombination reactions, they predict faster temperature and pressure drops during expansion than the nonequilibrium model. Also, because of the high tem-

turn results in a slower temperature and pressure decrease for the frozen model than the ideal-gas model.

5.5. *Convergence Property*

The convergence histories of the nonequilibrium calculations for three cases discussed earlier, i.e., the blunt-body flow, ramped-duct flow, and the divergent nozzle flow, are shown in Fig. 10 for both inviscid and viscous flows. The slow down of convergence in the ramped-duct case in viscous calculation is attributed to the presence of large scale flow separations. The running time of the viscous calculations, including integrating eight equations, calculating chemical source terms and thermophysical properties, is about 95.5 μ/grid point/time step on a CRAY-YMP computer, using the cft77 compiler. Overall, the efficiency (convergence rate and the cpu time/grid point/time step) and the robustness of the present method are very satisfactory.

As mentioned earlier, the maximum allowable CFL numbers for these calculations range between 2 to 10 and are limited by chemical kinetics rather than the stability of the numerical method. In fact, it was found in the present study that calculations using the ideal-gas model yield residuals

steps. The most severe CFL number limitation (CFL = 2) occurs in the case of hypersonic flow over a circular half-cylinder. In this case the density and temperature behind the bow shock increase considerably. Since in the present chemistry model the elemental chemical reaction rates are a function of density squared or cubed (ρ^2 or ρ^3, depending on the order of the reaction) and an exponential function of temperature, downstream of the shock the reaction rates become extremely large, rendering the species equations to be dominated by the chemical source terms. In this case, the meaning of the CFL number becomes less significant and the time step size is controlled by the need to resolve species concentration changes in this region. If too large a time step is used, undershoot or overshoot of species concentration occurs which destablizes the calculation, despite the implicit treatment of the source terms. To further clarify this issue, a test case was run with lower freestream pressure, i.e., $p_\infty = 0.01$ atm (as opposed to 1.0 atm used in Section 5.1). In this case the reaction rates are significantly reduced (by

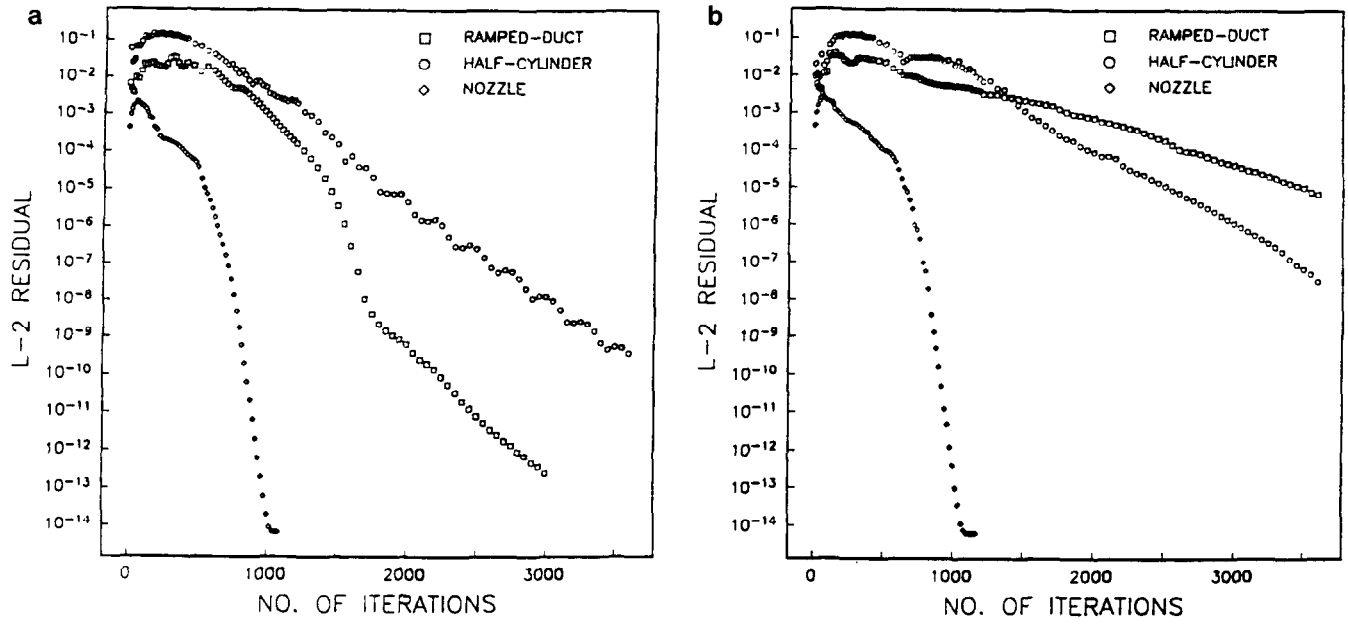

FIG. 10. Convergence histories of the present upwind method: (a) inviscid flows; (b) viscous flows.

a factor of 10^4 or more), and, as a result, the CFL number (time step size) can be increased to CFL = 5.0 without destablizing the computation.

Throughout the study, it is found that the Roe scheme requires about 20% more cpu time per time step than the Van Leer scheme, and the MUSCL differencing always converges faster than the flux differencing for the same flow. The superior convergence property of the MUSCL differencing can be attributed to the following reasons. As discussed in [27], the fluxes in MUSCL are split according to the local cell interface Mach number, whereas in the flux differencing approach the splitting depends on the Mach number at various cell interfaces. Also, the split fluxes are generally less differentiable than the flow variables when eigenvalues change signs [27].

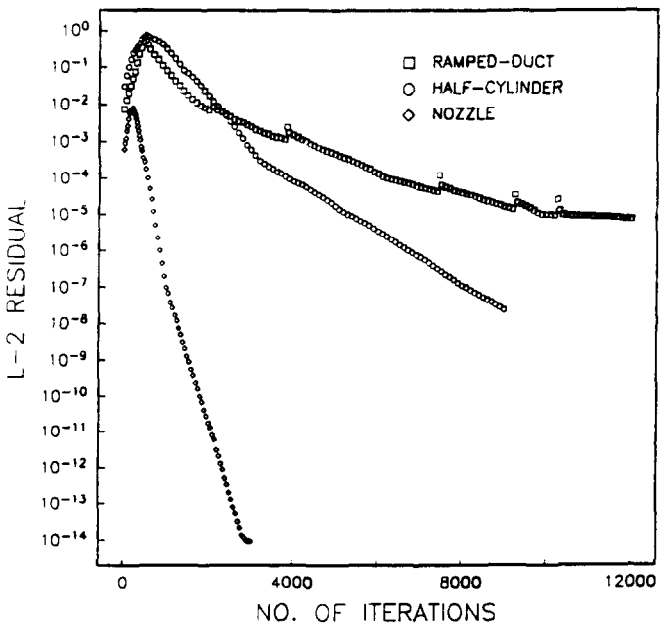

FIG. 11. Convergence histories of the LU-SGS method, viscous flows.

In recent years, the LU-SGS algorithm [19] has become quite popular for reacting flow calculations. As discussed in the Introduction, this method uses central difference for the explicit operator and one-sided difference for the implicit operator. In order to compare the relative efficiency of the present upwind algorithm with the LU-SGS method, numerical computations were also conducted using the LU-SGS method for some of the test flows considered in the present study. Only viscous cases are considered in the comparison and exactly the same grid distributions and boundary conditions as in the upwind calculations are used here.

The convergence histories of the LU-SGS algorithm are shown in Fig. 11. The running time is 62.4 μs/grid point/time step (on a CRAY-YMP computer, cft77 compiler), which is about 65% of that of the present upwind method. For the half-cylinder and divergent nozzle flows, the LU-SGS method takes about 2.5 times the number of iterations as the upwind method to converge to the same level of residuals. For the ramped-duct case, the LU-SGS method encounters very slow convergence, likely caused by the massive flow separations. Overall, the comparison favors the upwind method over the LU-SGS scheme in both efficiency and robustness accounts. Similar findings have also been reported in [34].

6. CONCLUDING REMARKS

We have presented a numerical method for solving the chemical nonequilibrium Navier–Stokes equations. The method is based on a finite-volume, upwind, TVD spatial discretization integrated by an upwind LU algorithm. Various test cases demonstrate the good shock-capturing capability as well as the efficiency and robustness of the method. Numerical results also show that the present method has the potential for calculating high speed nonequilibrium flows with complex wave structure. Work for further algorithm validation, expecially for the accuracy of the chemistry and the viscous formulation, is still needed and is being planned.

APPENDIX

$$\mathbf{S}_\xi = \begin{bmatrix} 1 & 0 & \frac{\rho}{\sqrt{2}a} & \frac{\rho}{\sqrt{2}a} & 0 & 0 & 0 & 0 \\ u & k_2\rho & \frac{\rho(u+k_1a)}{\sqrt{2}a} & \frac{\rho(u-k_1a)}{\sqrt{2}a} & 0 & 0 & 0 & 0 \\ v & -k_1\rho & \frac{\rho(v+k_2a)}{\sqrt{2}a} & \frac{\rho(v-k_2a)}{\sqrt{2}a} & 0 & 0 & 0 & 0 \\ H-\frac{\rho a^2}{p_e} & \rho(k_2u-k_1v) & \frac{\rho(H+\Theta)}{\sqrt{2}a} & \frac{\rho(H-\Theta)}{\sqrt{2}a} & \frac{-\rho^2 p_{C_1}}{p_e} & \frac{-\rho^2 p_{C_2}}{p_e} & \frac{-\rho^2 p_{C_3}}{p_e} & \frac{-\rho^2 p_{C_4}}{p_e} \\ Y_1 & 0 & \frac{\rho Y_1}{\sqrt{2}a} & \frac{\rho Y_1}{\sqrt{2}a} & \rho & 0 & 0 & 0 \\ Y_2 & 0 & \frac{\rho Y_2}{\sqrt{2}a} & \frac{\rho Y_2}{\sqrt{2}a} & 0 & \rho & 0 & 0 \\ Y_3 & 0 & \frac{\rho Y_3}{\sqrt{2}a} & \frac{\rho Y_3}{\sqrt{2}a} & 0 & 0 & \rho & 0 \\ Y_4 & 0 & \frac{\rho Y_4}{\sqrt{2}a} & \frac{\rho Y_4}{\sqrt{2}a} & 0 & 0 & 0 & \rho \end{bmatrix}, \tag{A.1}$$

$$\mathbf{S}_\xi^{-1} = \begin{bmatrix} 1-\frac{1}{a^2}\Phi & \frac{up_e}{\rho a^2} & \frac{vp_e}{\rho a^2} & -\frac{p_e}{\rho a^2} & -\frac{p_{C_1}}{a^2} & -\frac{p_{C_2}}{a^2} & -\frac{p_{C_3}}{a^2} & -\frac{p_{C_4}}{a^2} \\ -\frac{1}{\rho}(k_2u-k_1v) & \frac{k_2}{\rho} & -\frac{k_1}{\rho} & 0 & 0 & 0 & 0 & 0 \\ \frac{1}{\sqrt{2}\rho a}(-\Theta+\Phi) & \frac{1}{\sqrt{2}\rho a}\left(k_1a-\frac{up_e}{\rho}\right) & \frac{1}{\sqrt{2}\rho a}\left(k_2a-\frac{vp_e}{\rho}\right) & \frac{1}{\sqrt{2}\rho a}\frac{p_e}{\rho} & \frac{p_{C_1}}{\sqrt{2}\rho a} & \frac{p_{C_2}}{\sqrt{2}\rho a} & \frac{p_{C_3}}{\sqrt{2}\rho a} & \frac{p_{C_4}}{\sqrt{2}\rho a} \\ \frac{1}{\sqrt{2}\rho a}(\Theta+\Phi) & \frac{-1}{\sqrt{2}\rho a}\left(k_1a+\frac{up_e}{\rho}\right) & \frac{-1}{\sqrt{2}\rho a}\left(k_2a+\frac{vp_e}{\rho}\right) & \frac{1}{\sqrt{2}\rho a}\frac{p_e}{\rho} & \frac{p_{C_1}}{\sqrt{2}\rho a} & \frac{p_{C_2}}{\sqrt{2}\rho a} & \frac{p_{C_3}}{\sqrt{2}\rho a} & \frac{p_{C_4}}{\sqrt{2}\rho a} \\ -\frac{Y_1}{\rho} & 0 & 0 & 0 & \frac{1}{\rho} & 0 & 0 & 0 \\ -\frac{Y_2}{\rho} & 0 & 0 & 0 & 0 & \frac{1}{\rho} & 0 & 0 \\ -\frac{Y_3}{\rho} & 0 & 0 & 0 & 0 & 0 & \frac{1}{\rho} & 0 \\ -\frac{Y_4}{\rho} & 0 & 0 & 0 & 0 & 0 & 0 & \frac{1}{\rho} \end{bmatrix}, \tag{A.2}$$

where

$$\Theta = k_1 ua + k_2 va,$$
$$\Phi = p_\rho + \frac{pp_e}{\rho^2} - \frac{p_e}{\rho}(H - u^2 - v^2), \tag{A.3}$$

and k_1 and k_2 are the orientations of the interface of the two neighboring cells; i.e.,

$$k_1 = \frac{y_\eta}{\sqrt{x_\eta^2 + y_\eta^2}}, \qquad k_2 = \frac{-x_\eta}{\sqrt{x_\eta^2 + y_\eta^2}}. \tag{A.4}$$

The similarity matrices in the η-direction, $\mathbf{S}_\eta$ and $\mathbf{S}_\eta^{-1}$, are found by letting

$$k_1 = \frac{-y_\xi}{\sqrt{x_\xi^2 + y_\xi^2}}, \qquad k_2 = \frac{x_\xi}{\sqrt{x_\xi^2 + y_\xi^2}}. \tag{A.5}$$

in Eqs. (A.1) and (A.2).

REFERENCES

1. C. P. Li, NASA TM-58274, 1986 (unpublished).
2. G. V. Candler and R. W. MacCormack, AIAA Paper 88-511, 1988 (unpublished).
3. C. Park and S. Yoon, AIAA Paper 89-1974 (unpublished).
4. G. V. Candler, AIAA Paper 89-312, 1989 (unpublished).
5. J. L. Steger and R. F. Warming, *J. Comput. Phys.* **40**, 263 (1981).
6. B. Van Leer, Lecture Notes in Physics, Vol. 170 (Springer-Verlag, New York/Berlin, 1982), p. 507.
7. P. L. Roe, *J. Comput. Phys.* **43**, 357 (1981).
8. M. S. Liou and B. van Leer, AIAA Paper 88-624, 1988 (unpublished).
9. M. Vinokur and J. L. Montagne, *J. Comput. Phys.*, to appear.
10. Y. Liu and M. Vinokur, *J. Comput. Phys.* **83**, 373 (1989).
11. P. Collela and H. M. Glaz, *J. Comput. Phys.* **59**, 264 (1985).
12. B. Grossman and R. W. Walters, AIAA Paper 87-1117-CP, 1987 (unpublished).
13. P. Glaister, *J. Comput. Phys.* **74**, 382 (1988).
14. M. S. Liou, B. van Leer, and J. S. Shuen, *J. Comput. Phys.* **87**, 1 (1990).
15. J. S. Shuen, M. S. Liou, and B. van Leer, *J. Comput. Phys.* **90**, 371 (1990).
16. R. M. Beam and R. F. Warming, *J. Comput. Phys.* **22**, 87 (1976).
17. A. Jameson and E. Turkel, *Math. Comput.* **37**, 385 (1981).
18. A. Jameson and S. Yoon, *AIAA J.* **25**, 929 (1987).
19. J. S. Shuen and S. Yoon, *AIAA J.* **27**, 1752 (1989).
20. F. M. Williams, *Combustion Theory*, 2nd ed. (Benjamin/Cumming, Menlo Park, CA, 1985).
21. S. Gordon and B. J. McBride, NASA SP-273, 1976 (unpublished); NASA TM-86885, 1984 (unpublished).
22. R. C. Reid, J. M. Prausnitz, and B. E. Poling, *The Properties of Gases and Liquids*, 4th ed. (McGraw-Hill, New York, 1988).
23. M. G. Dunn and S. W. Kang, NASA CR-2232, 1973 (unpublished).
24. R. F. Warming, R. M. Beam, and B. J. Hyett, *Math. Comput.* **29**, 1037 (1975).
25. M. S. Liou and A. T. Hsu, AIAA Paper 89-1994, 1989 (unpublished).
26. M. S. Liou, AIAA Paper 87-355, 1987 (unpublished).
27. W. K. Anderson, J. L. Thomas, and B. van Leer, AIAA Paper 85-122, 1985 (unpublished).
28. Y. Moon and M. S. Liou, AIAA Paper 89-1980, 1989 (unpublished).
29. A. Ambrosio and A. Wortman, *ARS J.* **32**, 281 (1962).
30. F. S. Billig, *J. Spacecraft* **4**, 822 (1967).
31. R. M. Beam and R. F. Warming, *AIAA J.* **16**, 393 (1978).
32. M. S. Liou, *Int. J. Num. Methods Fluids* **9**, 747 (1989).
33. R. J. Hakkinen, I. Greber, L. Trilling, and S. S. Arbarbanel, NASA Memo-2-18-59W, 1959 (unpublished).
34. Y. L. P. Tsai and K. C. Hsieh, AIAA Paper 90-396, 1990 (unpublished).